Influence of bundle porosity on shell-side hydrodynamics and mass transfer in regular fiber arrays: A computational study

N. Cancilla[1], L. Gurreri[2*], M. La Rosa[1], M. Ciofalo[1], A. Cipollina[1], A. Tamburini[1], G. Micale[1]

[1]*Dipartimento di Ingegneria, Università degli Studi di Palermo, Viale delle Scienze Ed. 6, 90128 Palermo, Italy*

[2]*Dipartimento di Ingegneria Elettrica, Elettronica e Informatica, Università di Catania, Viale Andrea Doria 6 Ed. 13, 95125 Catania, Italy*

[*]corresponding author: luigi.gurreri@unict.it

Abstract

CFD predictions of the effects of a fiber bundle porosity on shell-side hydrodynamics and mass transfer under conditions of steady laminar flow were obtained. Fluid was assumed to flow around regular hexagonal or square arrays of cylindrical fibers of different pitch to diameter ratios, yielding bundle porosities ranging from the theoretical minimum up to ~1. A large number of axial, transverse and mixed flow combinations were simulated by letting the axial and transverse flow Reynolds numbers and the transverse flow attack angle vary. Both fully developed and developing conditions (entrance effects) were considered. The continuity and momentum equations, along with a transport equation for the concentration of a high-Schmidt number solute, were solved by a finite volume CFD code. Fully developed conditions were simulated by the well-established "unit cell" approach, in which the computational domain is two-dimensional and includes a single fiber with the associated fluid, periodic boundary conditions are imposed between all opposite sides and compensative terms are introduced to account for large-scale longitudinal or transversal gradients. Developing flow was studied by using a fully three-dimensional computational domain. Predictions were validated against experimental, computational and analytic literature results.

Keywords: *Computational Fluid Dynamics, hollow fiber membrane, entrance effects, Darcy permeability, mass transfer coefficient, hemodialysis.*

1. Introduction

Hollow fiber membranes are becoming increasingly common in many areas of membrane separation processes, such as direct capture of CO_2 [1], air humidification [2] extraction, for example, of heavy metals [3] or nitrogen-based liquid fertilizer [4] from wastewaters and gas separation [5], or in the wide field of water treatment and desalination processes [6], such as ultrafiltration, reverse osmosis and membrane distillation but also in several biomedical applications [7,8] (e.g., hemodialysis and blood oxygenators).

These membranes are typically used in bundles [9] of several thousand hollow fibers, enclosed in cylindrical modules as showed in **Figure 1**. The polymeric shell of a module can be made of polycarbonate or polypropylene. The bundle is bonded by means of an epoxy resin potting compound, which permits the two fluids to be segregated. Modules are provided with appropriate inlet/outlet ports for both the lumen- and the shell-side fluids and usually operate in counter-current flow to maximize mass transfer efficiency. The most common configuration foresees that the feed flows in the lumen side while the permeate flows in the shell side but also the opposite arrangement may be used.

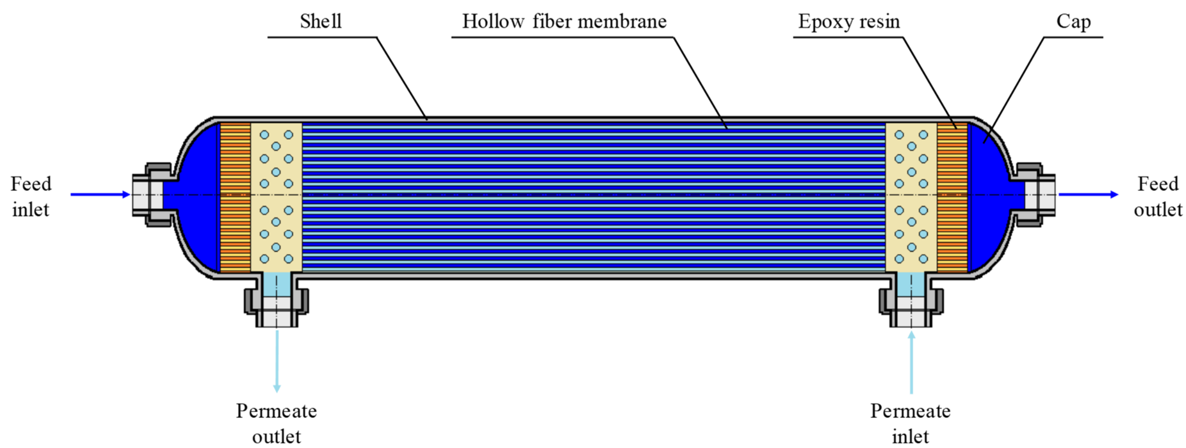

Figure 1: Schematic of a typical hollow fiber membrane module operating in counter-current flow.

The modelling of the lumen side flow is quite simple and is typically studied by the elementary Hagen-Poiseuille theory in regard to fluid dynamics and by semi-empirical correlations for mass transfer [10].

Due to the complexity of the geometry and of the resulting flow, the modelling of the shell side flow and mass transfer requires more than simple correlations. In particular, for mass transfer coefficients, several correlations [11–15] were developed in the past, but they yielded broadly dispersed values and were generally limited to few specific cases.

The study of hydrodynamics and mass transfer on the shell side is anything but trivial since it depends on many parameters.

The first parameter is the fiber arrangement, which can be described as a regular (hexagonal, square or, less commonly, rectangular) or irregular (random) lattice. Günther *et al.* [16] studied phenomena involving fluid flow and mass transfer in hexagonal fiber arrays while Eloot *et al.* [17] carried out simulations of a twelfth part of a fiber, always considering the bundle arranged in a hexagonal lattice. Also Cancilla *et al.* [18] simulated fluid flow and mass transfer around straight, axially indefinite, fibers arranged in regular square and hexagonal lattices. Dierickx *et al.* [19] studied three different configurations: in-line square, staggered square and equilateral triangle fiber arrays. The modelling of the fiber bundle in irregular arrays are less common in the literature. Zhang *et al.* [20] conducted numerical simulations in square, diagonal and random lattices and also Buetehorn *et al.* [21] assumed irregular fiber arrangements. Effects of the randomness on friction coefficients were also accounted for by Chen and Hlavacek [22]; Rogers and Long [23] and Wu and Chen [24] used the same approach also for mass transfer coefficients.

The second important parameter is the porosity of the bundle, i.e. the void fraction occupied by the shell side fluid. It is a continuous parameter and can vary from its theoretical minimum (when the center-to-center distance between two fibers is equal to their external diameter) to the theoretical maximum of 1. As early as in the 1920s, Emersleben [25] presented a theoretical analysis of the fluid dynamics of an infinite fluid surrounding a single fiber (porosity=1). Sullivan [26,27] studied experimentally the influence of the porosity on hydrodynamics for parallel and perpendicular flow around bundles of cotton fibers and of aligned cylinders. More recently, the effects of porosity were also investigated by various authors, *via* both numerical [28–30] and experimental [31–34] approaches.

The third and fourth parameters to be considered are the Reynolds numbers both in the direction of the fibers and in that perpendicular to them; their magnitude determines the fluid dynamics regime (e.g. laminar vs. turbulent), while their ratio specifies the relative importance of transverse velocity components with respect to the axial one. In regard to the former aspect, most operations using hollow fiber membranes are limited to laminar and stationary conditions; therefore, studies involving turbulence will not be discussed here. In regard to the latter aspect, most researchers limited their work only to axial flow [28,35–38], while less common are studies of transverse [39–41] or mixed flow [18,42].

A fifth controlling parameter is the transverse flow attack angle, whose influence characterizes the isotropy or anisotropy of the fiber lattice in regard both to hydrodynamics and mass transfer.

In [18] the angular dependence for both square and hexagonal lattices, in purely transverse and in mixed flow, was studied at a fixed porosity of 50%.

The sixth parameter, relevant only in the presence of mass (or heat) transfer, is the Schmidt (or Prandtl) number. Wilk [43] reported experimental results on mass and heat transfer processes occurring in mini-channels with small hydraulic diameters, along with many literature results, for different values of the Schmidt (or Prandtl) number. Antonopoulos [42], using a finite-difference method, solved the flow and heat transport governing equations for different values of the Prandtl number.

The seventh controlling parameter is the distance from inlet, often expressed in dimensionless form as a Graetz number: in fact, the development of velocity and concentration / temperature boundary layers (entrance effects) may heavily affect friction and mass / heat transfer. Few researchers investigated entry mass / heat transfer effects for laminar flow around regular [38,44] and random [45] arrays, while most studies have been limited to fully developed conditions [22,28,35,36]. As will be discussed in detail in Section 3.1.1, entry effects can be important in the presence of large Schmidt numbers, typical of most mass transfer processes.

Finally, the influence of the boundary conditions on mass / heat transfer (e.g., constant wall flux or constant wall concentration / temperature) deserves attention. For example, Miyatake and Iwashita [38,44] and Bao and Lipscomb [29,37] carefully investigated mass transfer around randomly arranged fiber bundles in axial flow, for both the uniform wall flux and the uniform wall concentration conditions.

Table 1 summarizes the above parameters and indicates (on the basis of the results obtained in the present work) the quantity or quantities more affected by their individual variation.

Table 1: Controlling parameters and affected quantities.

N.	Controlling parameter	Main quantities affected
1	Lattice type (square / hexagonal / random)	Hydrodynamics, mass transfer
2	Bundle porosity, ε	Friction and mass transfer coefficients
3	Axial Reynolds number, Re_z	Friction coefficient
4	Transverse Reynolds number, Re_t	Friction and mass transfer coefficients
5	Transverse flow attack angle, θ	Friction and mass transfer coefficients
6	Schmidt number, Sc	Mass transfer coefficient
7	Distance from inlet (entry effects)	Friction and mass transfer coefficients

The picture resulting from a combination of the above parameters is quite complex. Despite the large number of works concerning fluid flow and mass transfer around fiber arrays, a thorough study which takes into account most of the above mentioned parameters is still lacking.

In a previous paper [18], the influence of most of the above mentioned parameters was studied for a specific value of the bundle porosity ε (0.5). In the present work, the study is extended to different values of ε. The shell-side flow and mass transfer characteristics of both square and hexagonal regular lattices at different porosities will be illustrated. In addition, the influence of entry effects will be considered for selected configurations.

2. Models and methods

2.1 Modelling approach and general assumptions

Simulations of fluid flow and mass transfer around bundles of hollow fibers were conducted by means of the commercial finite volume (FV) code Ansys CFX-18®.

The fiber bundle was modelled based on the following simplifying assumptions:

1. All the fibers are the same in dimensions and properties;
2. Fibers are arranged in regular hexagonal or square arrays;
3. Fibers are straight along the longitudinal z axis;
4. In the fully developed region, no flow/concentration feature larger than a single unit-cell exists;
5. Fluid physical properties (density, dynamic viscosity) are constant (changes, associated with changes in concentration were estimated to be negligible);
6. Fluid flow is laminar and steady.

Assumptions (1)-(4) allowed simulations to be carried out by using the unit cell approach, in which the computational domain was a repetitive periodic unit of the bundle including a single fiber. This approach was already used by the authors in previous studies, e.g. [18].

Based on the above assumptions, the governing equations can be written as follows:

$$\vec{\nabla} \cdot \vec{u} = 0 \tag{1}$$

$$\rho \vec{u} \cdot \vec{\nabla} \vec{u} = -\vec{\nabla} p + \mu \nabla^2 \vec{u} + \vec{f} \tag{2}$$

in which $\vec{u}$ is the velocity, p is the pressure, ρ and μ are the density and the dynamic viscosity of the fluid and $\vec{f}$ is a forcing term (driving pressure gradient) compensating the large-scale pressure loss. Eqs. (1) and (2) are, respectively, the steady-state continuity and momentum equations for the flow of a Newtonian incompressible fluid.

The convection-diffusion transport equation governing the concentration field is:

$$\vec{u} \cdot \vec{\nabla} C = D \nabla^2 C + S_C \tag{3}$$

C being the concentration of the solute and D its diffusion coefficient in the fluid. S_C is a source term compensating the large-scale C gradient.

The fluid properties were set equal to those of pure water at 25°C (density ρ=997 kg·m^{-3} and dynamic viscosity μ=8.89·10^{-4} Pa·s [46]). The diffusion coefficient of the solute in the fluid was computed by assuming a Schmidt number $Sc=\mu/(\rho \cdot D)$=500. This value was selected as representative of a vast class of ionic (e.g. NaCl) and molecular (e.g. urea) solutes in water [47,48].

By using the above unit-cell approach, the computed $\vec{u}$, p and C are the periodic components of velocity, pressure and concentration so that periodic boundary conditions can be imposed to these variables between opposite boundaries of the computational domains. On the cylindrical wall of the fibers, the no slip condition was imposed to the velocity field and a Neumann boundary condition to the concentration field, with an arbitrary value of 10^{-5} mol m^{-2} s^{-1} for the wall mass flux. This choice, with respect to the possible alternative boundary condition (e.g. Dirichlet), better approaches the real operating conditions in a hollow fiber bundle: in most applications concerning membrane separation processes (e.g., hemodialysis), the resistance associated with the membrane is far larger than the others (lumen- and shell-side) and is circumferentially uniform around a fiber. Accordingly, the wall mass flux is expected to be almost uniform.

The simulations reported in this work were performed in double precision. A very tight convergence criterion was adopted: the dimensionless residuals of all quantities were imposed to be reduced below 10^{-12} for the solver to stop.

2.2 Definitions

In the present work, the porosity ε is defined as:

$$\varepsilon = \frac{V}{V_{tot}} \tag{4}$$

where V is the volume of the fluid and V_{tot} is the total volume, resulting by adding the volume of the fiber to V. The hydraulic diameter D_{eq} is defined as:

$$D_{eq} = \frac{4 \cdot V}{S} \tag{5}$$

in which S is the wet surface in the computational domain. It is easy to verify that, for any lattice, one has

$$\frac{D_{eq}}{d} = \frac{\varepsilon}{1-\varepsilon} \tag{6}$$

in which d is the diameter of the fibers. Eq. (6) shows that the hydraulic diameter diverges for $\varepsilon \to 1$.

Let $\vec{u}$ be the *superficial* velocity vector (porosity $\varepsilon \times$ local velocity). For consistency with our previous work and with most of the literature on the subject, only the superficial velocity will be adopted throughout this paper and no use will be made of the local, or *interstitial*, velocity. The Reynolds number Re_ξ along the generic direction ξ of unit vector $\vec{\xi}$ is defined as:

$$\mathrm{Re}_\xi = \frac{\rho \langle u_\xi \rangle D_{eq}}{\mu} \tag{7}$$

in which $\langle u_\xi \rangle$ is the volume average of the superficial velocity component along the generic direction ξ. In particular, Re_z will denote the Reynolds number along the axial direction z, while Re_t will denote the Reynolds number along a generic direction t lying in the cross-sectional plane.

Let now $\vec{\sigma} \equiv \vec{f} / |\vec{f}|$ be the unit vector characterizing the direction of the imposed forcing term and $\vec{\gamma} \equiv \langle \vec{u} \rangle / |\langle \vec{u} \rangle|$ the unit vector characterizing the direction of the mean (volume-averaged) superficial velocity. In general (hydrodynamically anisotropic medium), the directions $\vec{\gamma}$ and $\vec{\sigma}$ will *not* coincide.

The Darcy permeability K_σ along the direction $\vec{\sigma}$ of the imposed forcing term $\vec{f}$ is conventionally defined here as:

$$K_\sigma = \frac{\mu \langle u_\sigma \rangle}{|\vec{f}|} \tag{8}$$

In particular, K_z will denote the permeability along the axial direction, while K_t will denote the permeability along a generic direction lying in the cross-sectional plane.

In purely axial flow, the only imposed forcing term is f_z. In purely transverse flow, forcing terms in different directions lying in the bundle's cross sectional (xy) plane are imposed; the cross flow attack angle θ is conventionally defined as the angle between the forcing term $\vec{f}$ and the x axis (**Figure 2**). The transverse flow Reynolds number Re_t was computed on the basis of the mean (*superficial*) velocity $\langle u_t \rangle$ projected on the direction of the forcing term:

$$\langle u_t \rangle = \langle u_x \rangle \cos\theta + \langle u_y \rangle \sin\theta \tag{9}$$

in which $\langle u_x \rangle$ and $\langle u_y \rangle$ are the mean (*superficial*) velocities along the x and y directions.

In order to obtain mixed flow conditions, both an axial and a transverse forcing terms were imposed.

The average mass transport coefficient U is defined as:

$$U = \frac{\overline{J}}{\overline{C}_w - C_b} \tag{10}$$

where $\overline{J}$ is the wall-averaged molar flux at the wall, $\overline{C}_w$ is the wall-averaged solute concentration at the wall and C_b is the mass flow-weighted average of the solute concentration on an arbitrary cross section, i.e. the bulk concentration.

In the present work, two different definitions of the average Sherwood number were used, based to the fact that this quantity was made dimensionless on the basis of either the hydraulic diameter, $Sh_{D_{eq}}$:

$$Sh_{D_{eq}} = U \frac{D_{eq}}{D} \tag{11}$$

or the fiber diameter, Sh_d:

$$Sh_d = U \frac{d}{D} \tag{12}$$

This second definition of the Sherwood number can be viewed as a porosity-independent dimensionless form of the mass transfer coefficient U.

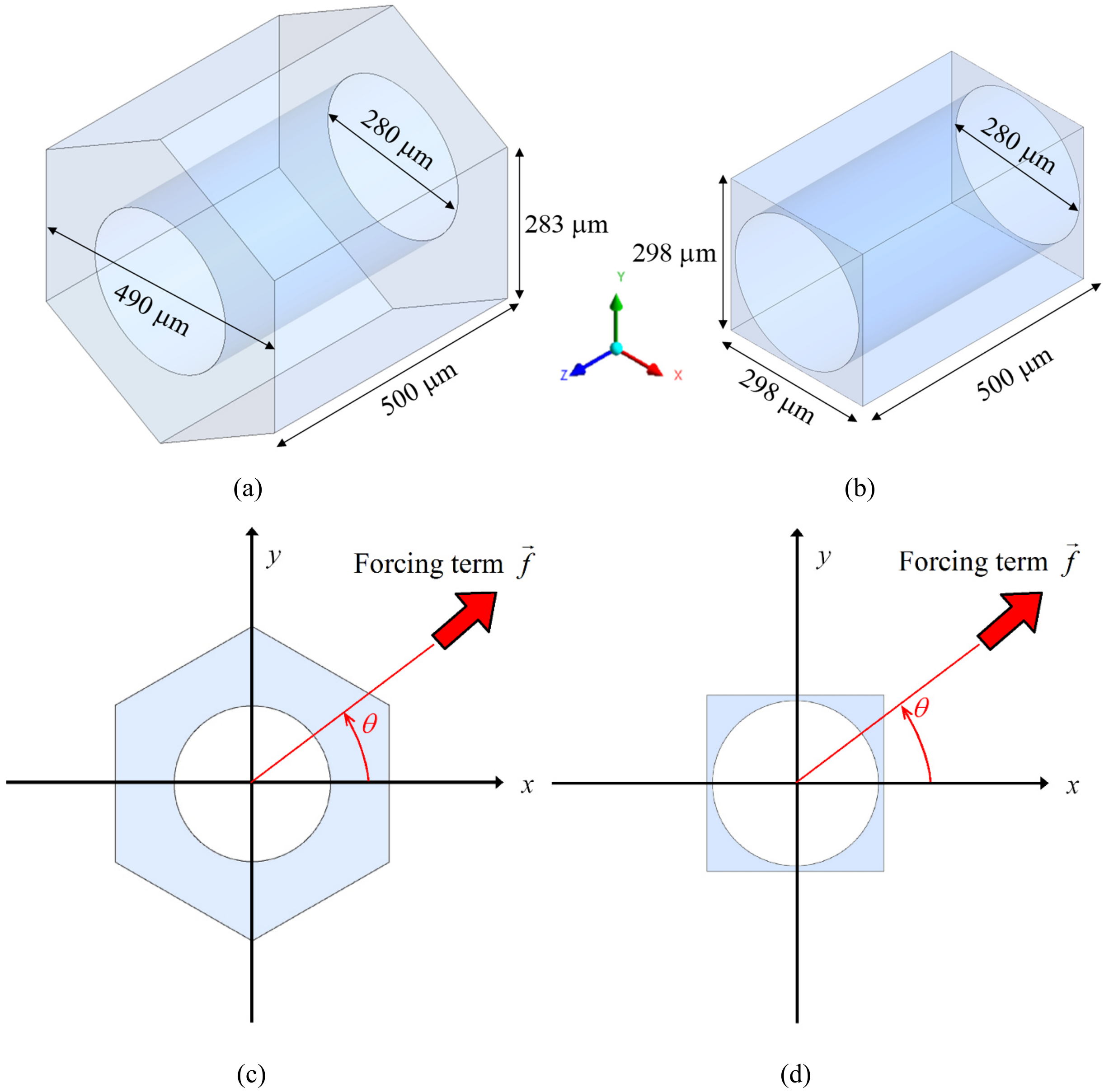

Figure 2: Geometries of (a, c) a hexagonal regular lattice with porosity ε=0.7 and (b, d) a square regular lattice with porosity ε=0.3. (a), (b) 3-D unit cells (computational domains); (c), (d) 2-D cross sections. The dimensions specified are for a typical hemodialysis module. The direction of the forcing term $\vec{f}$ and the cross-flow attack angle θ are also indicated.

2.3 Computational domains and finite volume grids

The simulations conducted in the present work can be divided into two categories, according to whether fully developed or developing conditions were imposed. These two different conditions imply a different dimensionality of the computational domains.

The former ones, aimed at studying the effects of different porosities on Darcy permeability and mass transfer coefficient, were essentially two-dimensional and the extent of the computational domains along the longitudinal direction was irrelevant. For compatibility with the computational code, it was arbitrarily set to 500 μm and was discretized by three finite volumes.

The computational grids were composed of hexahedral volumes only, known to provide more accurate results than tetrahedral or hybrid grids [49]. As reported in [18], grids of ~10,000 volumes in the *xy* plane provided results for the friction and mass transfer coefficients differing less than 1% from those obtained with the finest grid tested (~128,000 volumes in the *xy* plane). Conservatively, grids having up to ~100,000 volumes in the *xy* plane were adopted.

Developing flow simulations, focused on the study of entry effects, were intrinsically three-dimensional. Thus, the geometry was appropriately extended along the *z* direction so as to reach the fully developed flow and mass transfer limits. The grid was limited to ~10,000 volumes in the *xy* plane and included ~400 volumes along the axial direction *z* and was selectively refined near the channel inlet. Thus, the overall number of finite volumes was $\sim 4 \cdot 10^6$.

Figure 2 shows, as an example, two among the geometries used to carry out the following simulations, respectively for the hexagonal array of porosity 70% and for the square array of porosity 30%. The dimensions of the unit-cell and the outer diameter *d* of the fibers (arbitrarily set to 280 μm, a value typical of hemodialysis), are reported.

3. Results

In order to facilitate the comparison with the literature, in the present work K_σ is expressed in dimensionless form as a normalized Darcy permeability K_σ/d^2, where d is the fiber diameter. Values for K_z/d^2, K_t/d^2 and the average Sherwood numbers were computed by CFD for regular hexagonal and square arrays of different porosities, in order to assess the influence of this parameter on the results. Results are presented according to the considered flow condition (axial, transverse or mixed flow). In axial flow, entry effects were also accounted for. In transverse and mixed flow, the complex influence of the cross flow attack angle was carefully investigated.

3.1 Purely axial flow

In purely axial flow, only a forcing term along the longitudinal (z) direction was applied. In this parallel flow condition, neither the Darcy permeability nor the Sherwood number depend on the longitudinal Reynolds number (Re_z). Therefore, the simulations in purely axial flow were carried out at the arbitrary value Re_z=10, typical of several applications (e.g. hemodialysis modules).

3.1.1 *Hydrodynamics in purely axial flow*

Figure 3 reports in a semi-logarithmic chart the normalized Darcy permeability in the axial direction *z* (K_z/d^2) as a function of the porosity (ε) for both the hexagonal and the square lattices. Note that the curves start from two different values of porosity: according to the geometrical configuration of the fiber bundle arranged in the hexagonal and square arrays, the minimum ε-value (corresponding to a center-to-center distance between two fibers equal to the fiber diameter) is $\varepsilon\approx0.09$ for the hexagonal lattice and $\varepsilon\approx0.22$ for the square lattice. The maximum value of ε was arbitrarily set to 0.99 in both cases.

For both lattices, the normalized axial Darcy permeability grows about exponentially with ε up to $\varepsilon\approx0.8$-0.9 and overexponentially for larger ε, and diverges for $\varepsilon\rightarrow1$. In the range of ε investigated, for the hexagonal lattice K_z/d^2 ranges between 7.61×10^{-5} and 8.36 and, for the square lattice, between 1.27×10^{-3} and 19.8. The two curves practically merge for $\varepsilon>\sim0.7$.

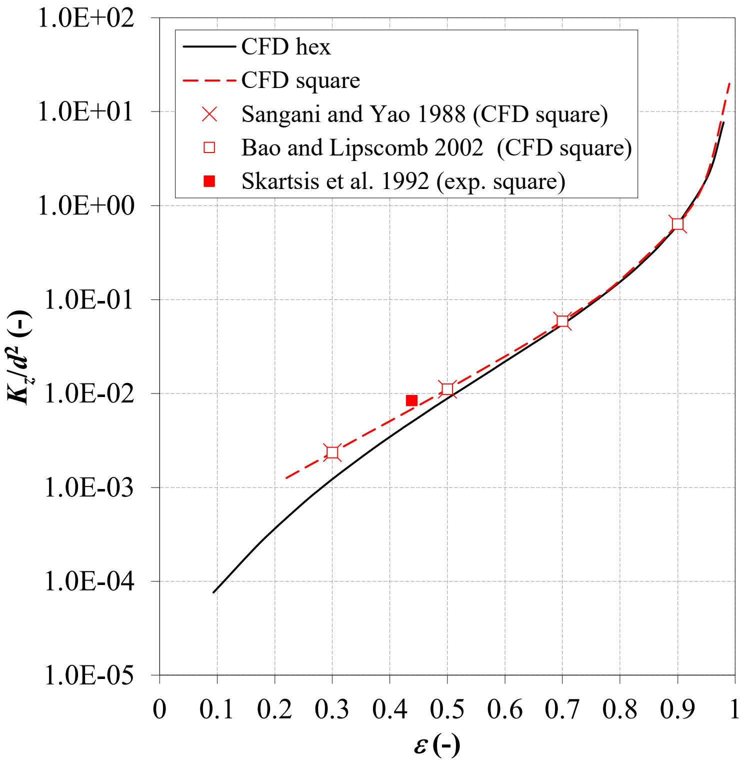

Figure 3: Normalized Darcy permeability along the axial direction predicted by CFD as a function of the porosity for regular hexagonal (solid line) and square (broken line) fiber arrays. Experimental and CFD results from the literature (symbols) are also reported for comparison purposes.

Results for square arrays exhibit an excellent agreement with numerical solutions reported by Sangani and Yao [50] and Bao and Lipscomb [29]. In [34] Skartsis *et al.* carried out experiments in axial flow using a special test section with aligned cylinders arranged in a square array and a porosity of ~44%. The relevant experimental value is reported in **Figure 3** as a solid symbol and is also in good agreement with the present CFD predictions.

3.1.2 Mass transfer in purely axial flow

In regard to mass transfer in purely axial flow, **Figure 4** reports, for both the hexagonal and the square lattices, the Sherwood number predicted as a function of the porosity, as defined on the basis of (a) the fiber diameter, Eq. (12) and (b) the hydraulic diameter, Eq. (11).

The curves of Sh_d, **Figure 4**(a), show bell-shaped behaviors, with a maximum of ~12 at $\varepsilon\approx0.38$ for the hexagonal lattice and of ~5 at $\varepsilon\approx0.6$ for the square lattice. The reason is that, at low porosities, the fibers are so close to one another that mass transfer is impaired; at high porosities, the thickness of the concentration boundary layer surrounding each fiber (and thus the mass transfer resistance) is very large. Therefore, in order to maximize the shell-side mass transfer, a good practice would be to choose porosities in the intermediate range between ~0.3 and ~0.5 for hexagonal arrays and between ~0.5 and ~0.7 for square arrays.

On the other hand, curves of $Sh_{D_{eq}}$ start at very low values (even < 1) for the lowest porosities and increase monotonically as the porosity increases, as a consequence of the increase in D_{eq}, Eq. (6). In particular, up to a porosity $\varepsilon\approx0.8$-0.9 the curve for the hexagonal lattice lies significantly above that for the square lattice, whereas for larger values of ε the two curves collapse into a single behavior. As the permeability, also the Sherwood number $Sh_{D_{eq}}$ diverges for $\varepsilon\rightarrow1$.

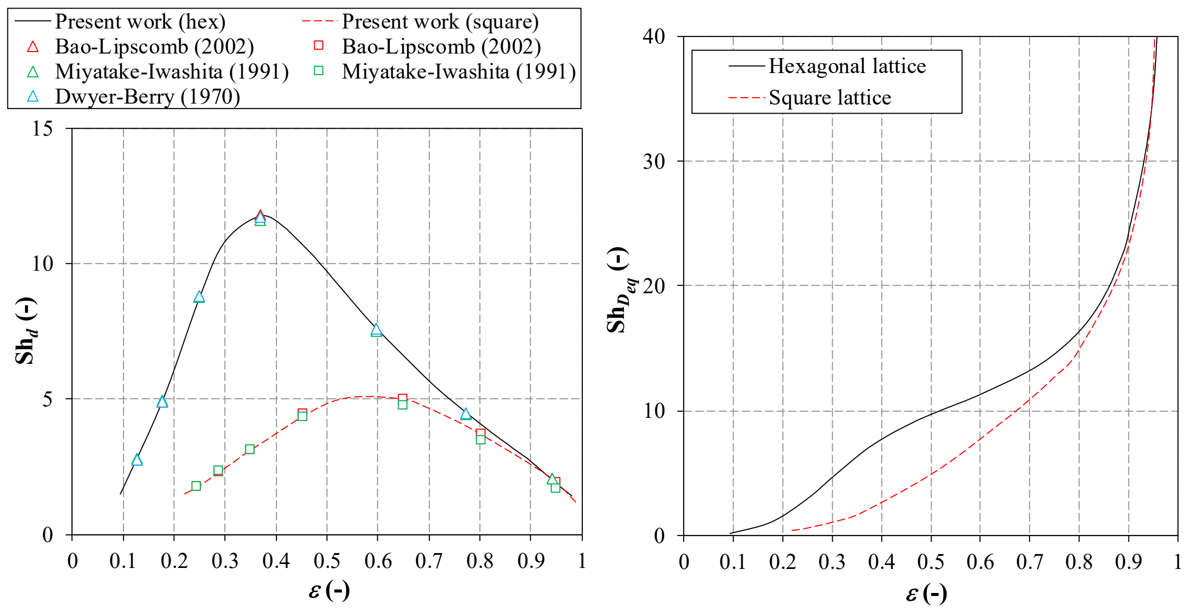

(a) (b)

Figure 4: Sherwood number predicted by CFD as a function of the porosity for regular hexagonal (solid line) and square (broken line) fiber arrays. (a) Sh_d, defined on the basis of the fiber diameter; (b) $Sh_{D_{eq}}$, defined on the basis of the hydraulic diameter. Computational results from the literature for regular hexagonal and square arrays (triangular and square symbols, respectively) are also reported for comparison purposes.

Figure 4(a) shows also the comparison between the present predictions (solid line for hexagonal lattice, broken line for square lattice) and some computational results reported by various authors (symbols). In particular, for the hexagonal lattice the predictions agree very well with results by Bao and Lipscomb [37], Miyatake and Iwashita [38] and Dwyer and Berry [28]. Also for the square lattice, the present predictions are in good agreement with the results of Bao and Lipscomb [37] and Miyatake and Iwashita [38].

3.1.3 Entry effects in purely axial flow (square lattice)

Hydrodynamic entry effects for laminar flow in ducts have been for several decades the subject of intense research based either on experiments or on analytical or semi-analytical solutions of different simplified forms of the governing equations. Shah [51] proposed an empirically-based correlation for the friction coefficient in the entry region of circular, rectangular, equilateral triangular and annular ducts. Sparrow and co-workers [52,53], Langhaar (reported in [54]) and several other authors developed approximate solutions based on neglecting axial momentum diffusion and/or nonlinear terms in the Navier-Stokes equations.

Since the present geometry (fiber bundle) is significantly different from those considered the above mentioned works, CFD simulations of developing flow were run to estimate hydrodynamic entry effects in fiber bundles. For simplicity, the study was limited to the square lattice.

For this purpose, the computational domain was obtained by extruding a square-lattice unit cell like that shown in **Figure 2**(b). CFD simulations in developing flow were performed with computational domains having porosities of 0.31, 0.50 and 0.69. Periodic boundary conditions were imposed to all the lateral surfaces of the domain, while a uniform velocity was imposed at the *inlet* and an arbitrary pressure at the *outlet*. The cylindrical surface of the fiber was treated as a no slip wall.

Results for Re_z=10 are reported in **Figure 5** in the form of the ratio between the axial Darcy permeability and its fully developed value ($K_z/K_{z\infty}$) as a function of the dimensionless distance from inlet ($z/(Re_z \cdot D_{eq})$). It can be observed that the hydrodynamic entry effects depend on the porosity, with a more marked influence of this parameter for the lower values. In particular, at ε=0.69 one has $K_z/K_{z\infty}$=0.99 for $z/(Re_z \cdot D_{eq}) \geq \sim 0.05$, a length which corresponds to ~5 D_{eq} (≈3 mm in a bundle of fibers with diameter d=0.3 mm). At ε=0.50 the same value of $K_z/K_{z\infty}$ is reached for $z/(Re_z \cdot D_{eq}) \geq \sim 0.15$, corresponding to ~15 D_{eq} (≈4 mm). Finally, at ε=0.31 the condition $K_z/K_{z\infty}$=0.99 is touched for a value that is further forward along the z axis ($z/(Re_z \cdot D_{eq}) \geq \sim 0.5$, corresponding to $z \approx 50$ D_{eq} (≈6 mm). Note that, for any given d, values of D_{eq} are different for each porosity considered.

Therefore, hydrodynamic entry effects were found to be limited to a small region of the bundle, between 3 and 6 mm, a length utterly negligible with respect to the module length in most applications.

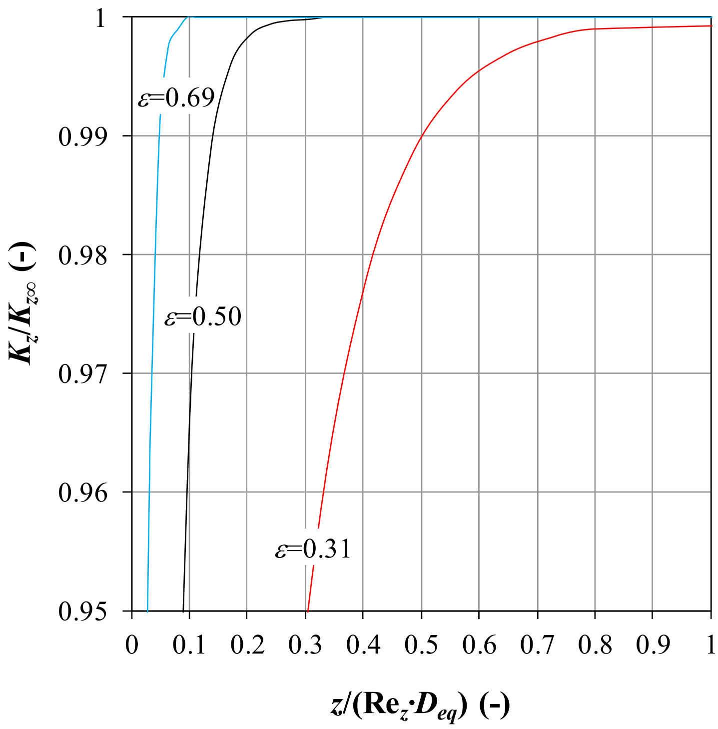

Figure 5: Axial Darcy permeability (K_z), normalized by its fully developed value ($K_{z\infty}$), as a function of the dimensionless distance from inlet ($z/(\mathrm{Re}_z \cdot D_{eq})$) for three different values of the porosity at $\mathrm{Re}_z \approx 10$.

In regard to mass transfer, entry effects are particularly important in the presence of large Schmidt numbers, because in this case the Péclet number may well be very large, so that the entry length becomes comparable or even larger than the size of the mass exchange unit.

For pipes and other straight channels with uniform cross section, entry effects on heat / mass transfer have been extensively studied on the basis of different analytical [54,55], computational [56–58] and experimental [56] results. Solutions differ according to whether hydrodynamically fully developed conditions (Graetz problem proper) or simultaneously developing flow and concentration / temperature fields are assumed, and to the boundary conditions imposed (uniform wall concentration / temperature, uniform wall mass / heat flux or more complex ones). In general, solutions depend also on the Péclet number $\mathrm{Pe}_z = \mathrm{Re}_z \cdot \mathrm{Sc}$. However, once the Sherwood number is reported as a function of the dimensionless variable $1/\mathrm{Gz} = z/(\mathrm{Pe}_z \cdot D_{eq})$ (reciprocal of the Graetz number), entry effects become independent of the Péclet number (and, *a fortiori*, of Re_z and Sc separately) for $\mathrm{Pe}_z >\sim 100$. The reason is that, at large Pe_z, the axial conduction term in the mass transport equation, which is the only term depending on Pe_z (as $1/\mathrm{Pe}_z^2$), becomes negligible.

For the present fiber bundle configuration, CFD simulations were performed for the three porosities investigated. The (irrelevant) Re_z and Sc numbers were arbitrarily assumed to be 10 and 500, respectively (typical of a hemodialysis module), yielding Pe_z=5000. Results in **Figure 6** report the dependence of the Sherwood number based on the hydraulic diameter ($Sh_{D_{eq}}$) upon the dimensionless variable 1/Gz.

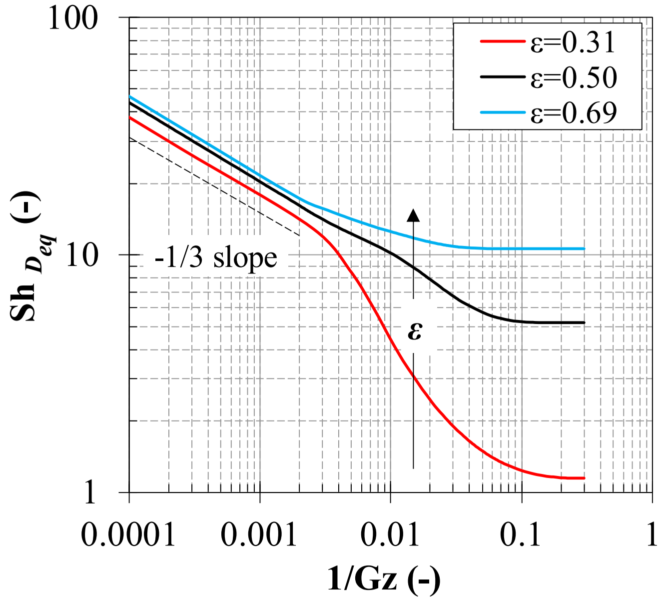

Figure 6: Sherwood number $Sh_{D_{eq}}$, defined on the basis of the hydraulic diameter, as a function of the reciprocal of the Graetz number (1/Gz), for three different values of the porosity ε.

In the whole range of 1/Gz, higher value of $Sh_{D_{eq}}$ are attained for higher porosities ε; the influence of ε is largest at high values of 1/Gz (fully developed conditions). In the double-logarithmic charts, the curves for all porosities exhibit the same linear trend with slope = -1/3 in the range $10^{-4}<1/Gz<2\cdot10^{-3}$, which corresponds to the region very close to the inlet. The dimensionless mass transfer development length, defined as the distance at which $Sh_{D_{eq}}$ is 1% larger than its fully developed value, decreases from ~0.2 to ~0.1 and ~0.04 as ε increases from 0.31 to 0.50 and 0.69, respectively. For the reference dimensions reported in **Figure 2** and Pe_z=5000, these values correspond at all porosities to a physical development length of ~0.13 m; for most commercial hemodialysis modules, this is a large fraction of the total length. Consistently, the fully-developed values of $Sh_{D_{eq}}$ reached as results of the above simulations in developing flow coincide exactly with results from unit-cell simulations in a square array at the same porosity (cf. broken line of **Figure 4**(a)). They are 1.14, 5.15 and 10.6 for porosities of 0.31, 0.50 and 0.69, respectively.

3.2 Purely transverse flow

In order to establish purely transverse flow, a forcing term lying in the *xy* cross sectional plane was applied.

3.2.1 Hydrodynamics in purely transverse flow

As far as the hydraulic permeability K_t is concerned, at sufficiently low values (<~10) of the transverse flow Reynolds number Re_t (defined in Section 2.2), K_t does not depend on Re_t nor on the flow attack angle θ (i.e., the medium is Darcian and is isotropic with respect to directions lying in a cross-sectional plane). In this range, the dependence of K_t on the porosity ε was investigated at an arbitrary transverse flow Reynolds number of 1 and an arbitrary flow attack angle of 0°.

Figure 7 reports in a semi-logarithmic chart the Darcy permeability in the transverse direction *t* as a function of the porosity (ε) for both the hexagonal and the square lattices. As for the axial permeability in **Figure 3**, K_t is normalized by the square of the fiber diameter *d*.

For both the square and the hexagonal lattices, K_t/d^2 rises about exponentially with the porosity from $\varepsilon\approx0.6$ to $\varepsilon\approx0.8$, underexponentially for $\varepsilon<0.6$ and overexponentially for $\varepsilon>0.8$; as expected, it diverges for $\varepsilon\to1$. Unlike the longitudinal permeability (**Figure 7**), the transverse permeability is larger at all porosities for the hexagonal lattice than for the square one; the difference is larger at low porosities, whereas the two curves practically coincide for $\varepsilon>\sim0.6$.

The present CFD predictions were compared with literature experimental results (symbols in **Figure 7**) reported by Bergelin *et al.* [31] and by Kirsch and Fuchs [32]: for both the square and the hexagonal arrays the curves obtained by CFD agree very well with the experiments. Skartsis *et al.* [34] carried out experiments in transverse flow using a special test section with aligned cylinders arranged in a square array and a porosity of ~46%. Also this experimental value is shown as a solid symbol in **Figure 7** and is in excellent agreement with the CFD predictions for this porosity.

The behavior of the normalized transverse Darcy permeability is qualitatively similar to that of the longitudinal permeability in **Figure 3**. However, transverse permeabilities are lower at all porosities than longitudinal permeabilities, the difference being largest at low ε.

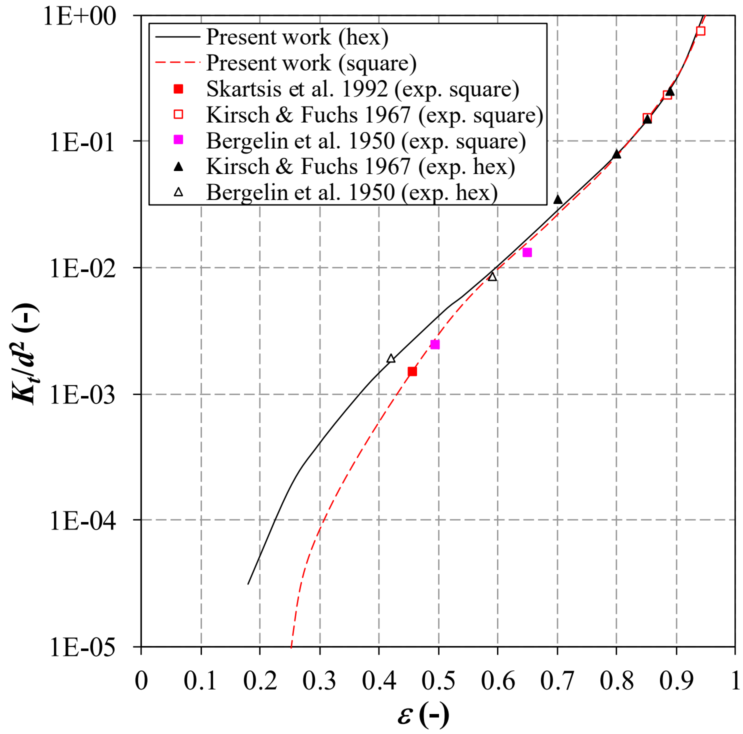

Figure 7: Normalized Darcy permeability along the transverse direction predicted by CFD as a function of the porosity for regular hexagonal (solid line) and square (broken line) fiber arrays in purely transverse flow. Experimental results from the literature (symbols) are also reported for comparison purposes.

3.2.2 Mass transfer in purely transverse flow

In regard to mass transfer in purely transverse flow, even at very low transverse flow Reynolds numbers Re_t, the Sherwood number is a function both of Re_t and of the flow attack angle θ. **Figure 8** shows the predicted Sherwood number, based on the fiber diameter d, as a function of the porosity for the hexagonal and square lattices at Re_t=1. In both cases, the cross-flow attack angle θ is 0°; qualitatively similar behaviors are obtained for other angles and transverse flow Reynolds numbers. The influence of Re_t and θ will be better illustrated in Section 3.3 (mixed flow).

As for the purely axial flow condition, **Figure 4**(a), also in purely transverse flow the curves of Sh_d exhibit a maximum. In particular, for the hexagonal lattice the maximum value of Sh_d is ~12.6 and is attained at ε≈0.25. For the square lattice, Sh_d attains a maximum of ~5.5 at ε≈0.45. The reasons for the occurrence of a maximum are the same discussed for the purely axial flow case. As in that case, the Sherwood numbers based on the hydraulic diameter exhibit a monotonic increasing behaviour and have not been reported.

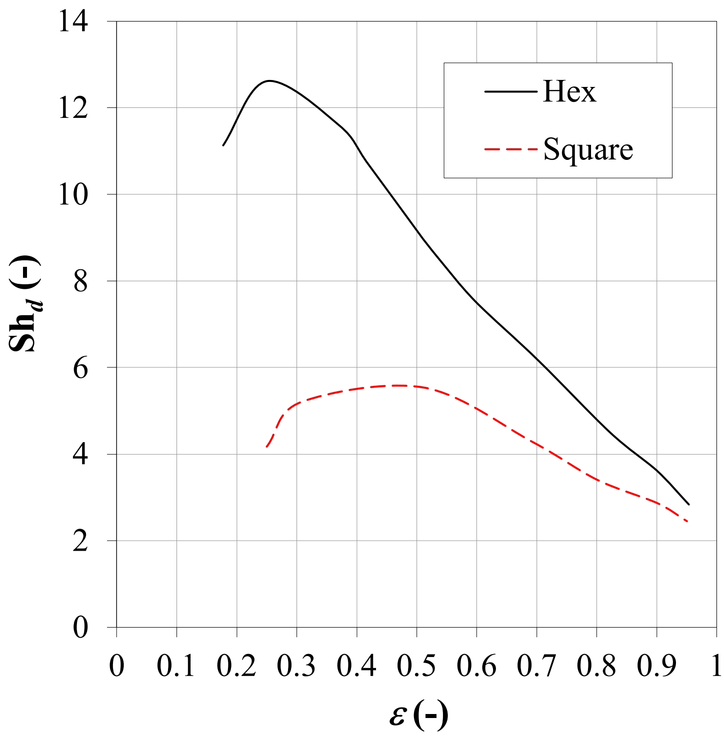

Figure 8: Sherwood number Sh_d, defined on the basis of the fiber diameter, as a function of the porosity in purely transverse flow for regular hexagonal and square fiber arrays for a transverse flow Reynolds number Re_t=1 and a cross-flow attack angle θ=0°.

3.3 Mixed flow

Under mixed flow conditions, the number of parameters to be considered rises: for each lattice type, the parameters involved are the porosity ε, the axial and transverse flow Reynolds numbers Re_z and Re_t along with the cross-flow attack angle θ.

A full parametrical study was prohibitive. Therefore, simulations were run for only three values of the porosity (31%, 50% and 69% for the square lattice, 30%, 50% and 60% for the hexagonal lattice), a few combinations of axial and transverse Reynolds numbers (in particular, Re_z=0, i.e. purely transverse flow, or Re_z=100 and $10^{-3}<Re_t<30$) and three different flow attack angles θ (0°, 22.5° and 45° for the square lattice, 0°, 15° and 30° for the hexagonal lattice). The values of θ were chosen so as to include, for each lattice, the two main directions of symmetry and an intermediate one.

Notably, as it is well-known from the literature [59], for $Re_t \geq 49$ phenomena of vortex shedding start to occur in the fluid and the assumption of steady-state flow fails. In order to avoid the complications of time-dependent solutions, only values of $Re_t \leq 30$ were considered in the present study.

3.3.1 Hydrodynamics in mixed flow

Figure 9 reports the normalized values of the Darcy permeability as a function of the transverse flow Reynolds number for a regular square lattice in mixed flow with Re_z=100 at different cross-flow attack angles θ. In particular, graph (a) is for K_z/d^2 (axial direction) and graph (b) is for K_t/d^2 (transverse direction).

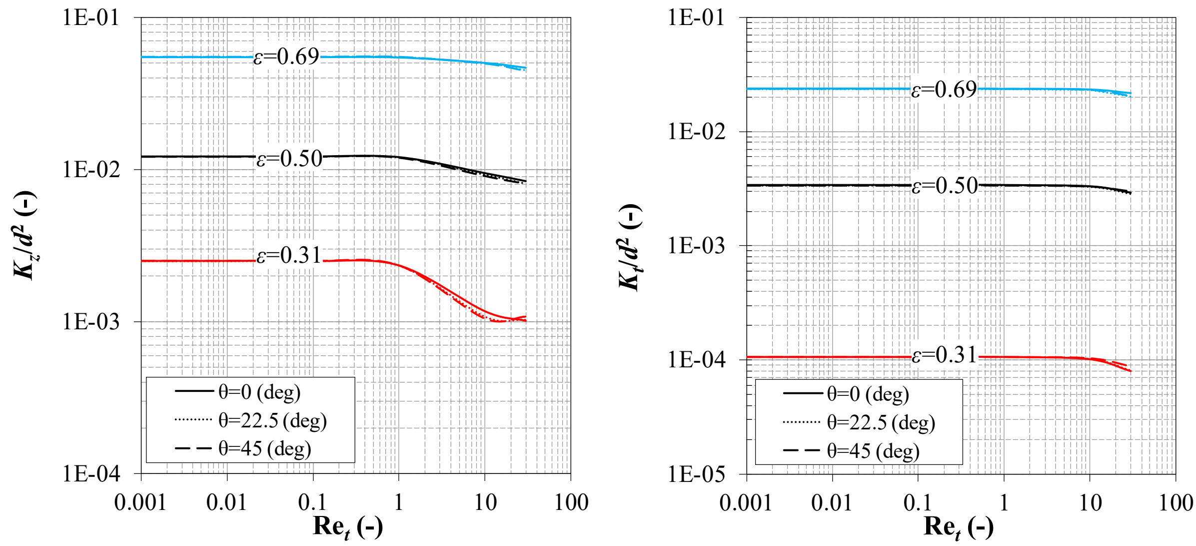

(a) (b)

Figure 9: Square fiber arrays: normalized Darcy permeability along (a) the axial (K_z/d^2) and (b) the transverse (K_t/d^2) direction predicted by CFD as a function of the transverse flow Reynolds number Re_t in mixed flow at Re_z=100. Three flow attack angles are considered: θ=0° (solid line), θ=22.5° (dotted line) and θ=45° (broken line).

Let us first discuss the way in which the simultaneous presence of the transverse flow affects the axial Darcy permeability, **Figure 9**(a). In general, the higher the porosity, the higher the ratio K_z/d^2. For each porosity, the curve departs from its constant low-Reynolds number value only for Re_t>~1. The most important influence of the presence of cross flow is observed at the lowest porosity (ε=0.31): the simultaneous presence of a transverse flow with Re_t=10 reduces K_z/d^2 by ~2.5 times. At ε=0.50 this reduction is only ~1.6 times and at ε=0.69 is ~1.2 times. The effects of the cross-flow angle θ are very small and can be appreciated only for the lowest porosity investigated.

Consider now **Figure 9**(b), which reports the normalized transverse Darcy permeability K_t/d^2, still as a function of the transverse Reynolds number Re_t, in mixed flow at Re_z=100 for three porosities. For the three porosity considered, K_t/d^2 departs from its constant value only for Re_t>~10; for Re_t≈30 it decreases by ~25% at ε=0.31 and by ~10% at ε=0.50 or 0.69. The influence of the cross-flow attack angle is negligible.

The corresponding curves computed in the absence of axial flow are completely coincident with those reported, showing that the transverse Darcy permeability K_t, is completely unaffected by the presence of an axial flow despite the significant value of Re_z (=100), in the whole Re_t range considered and for all values of ε and θ investigated. In particular, for Re_t<~10, values of K_t/d^2 coincide with those reported for purely transverse flow in **Figure 7** at the corresponding porosity.

Equivalent graphs for the hexagonal lattice are reported in **Figure 10**.

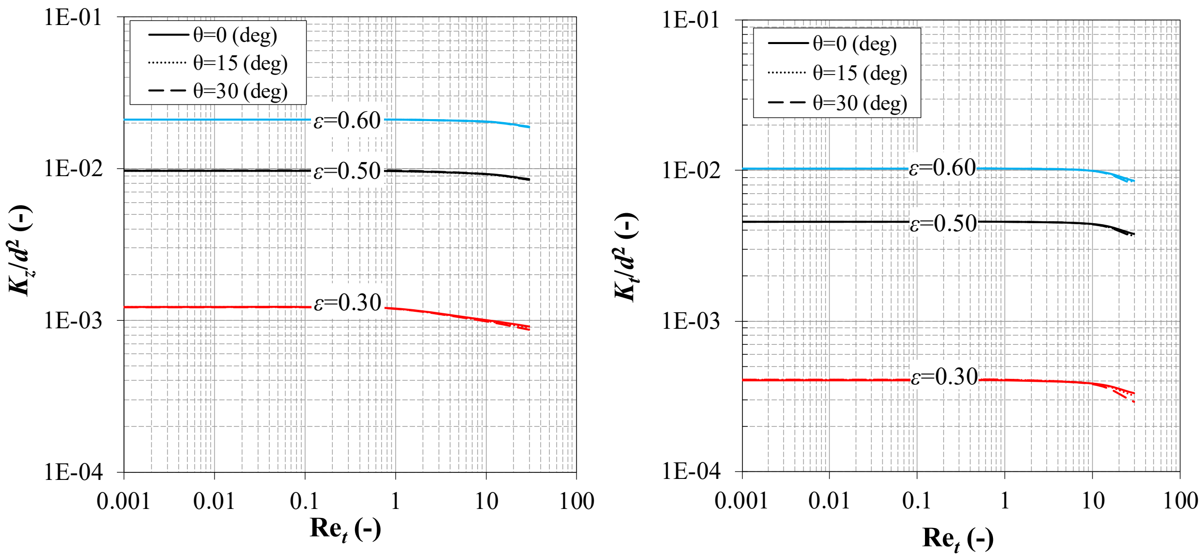

(a) (b)

Figure 10: Hexagonal fiber arrays: normalized Darcy permeability along (a) the axial (K_z/d^2) and (b) the transverse (K_t/d^2) direction predicted by CFD as a function of the transverse flow Reynolds number Re_t in mixed flow at Re_z=100. Three flow attack angles are considered: θ=0° (solid line), θ=15° (dotted line) and θ=30° (broken line).

Qualitatively similar behaviors to those of the square lattice are obtained also for the hexagonal lattice and similar considerations apply. In regard to the influence of cross flow on the longitudinal permeability, **Figure 10**(a), values of K_z/d^2 are constant up to Re_t≈1 and then tend to decrease. The most evident cross-flow influence is observed for the lowest porosity (ε=0.30), when, for Re_t≈30, K_z/d^2 decreases by ~36%; at ε=0.50 and ε=0.60 the decrease is less marked (~15% and 12%, respectively). The influence of cross flow is much less important than in the square lattice.

In regard to the transverse permeability K_t/d^2, **Figure 10**(b), the curves for the hexagonal lattice are qualitatively very similar to those obtained for the square lattice. The departure from the constant low-Reynolds number values ($K_t/d^2 \approx 4.0\times10^{-4}$ for ε=0.30, 4.5×10^{-3} for ε=0.50 and 1.0×10^{-2} for ε=0.60) starts at $Re_t \approx 10$. For $Re_t \approx 30$, values of K_t/d^2 decrease by ~38% at ε=0.30, by ~21% at ε=0.50 and by ~18% at ε=0.60.

The effects of θ on both the axial and transverse Darcy permeability are negligible: also the hexagonal lattice is hydraulically isotropic for the values of Re_z, Re_t and porosity investigated. From the results in **Figures 9-10** one may conclude that for both lattices, in the parameter range investigated, the axial permeability is not affected by the axial Reynolds number Re_z but is significantly affected by the transverse Reynolds number Re_t provided Re_t>~1, especially at low porosities. On the other hand, the transverse permeability is not affected by the axial flow Reynolds number Re_z and is only marginally affected by the transverse flow Reynolds number Re_t provided Re_t>~10.

3.3.2 Mass transfer in mixed flow

Figure 11 reports in log-log scale the Sherwood number as a function of the transverse flow Reynolds number for a regular square lattice for Re_z=100 (mixed flow) and Re_z=0 (purely transverse flow), for the three porosities analyzed and θ=0°. In particular, in graph (a) the Sherwood number is normalized by the hydraulic diameter as $Sh_{D_{eq}}$ while, in graph (b), it is normalized by the fiber diameter as Sh_d.

Let us first discuss the behavior of $Sh_{D_{eq}}$ in **Figure 11**(a). Both in mixed flow and in purely transverse flow, and for all porosities, $Sh_{D_{eq}}$ grows as the transverse Reynolds number increases. $Sh_{D_{eq}}$ does not follow a power law trend but exhibits a larger increase for Re_t>~1; the rate of increase is higher the lower the porosity. For given Re_t and Re_z, $Sh_{D_{eq}}$ increases monotonically with the porosity. Consider, for example, the cases of purely transverse flow (Re_z=0, solid lines): at Re_t=10, CFD predicts $Sh_{D_{eq}} \approx 4$ at ε=0.31, $Sh_{D_{eq}} \approx 6.8$ at ε=0.50 and $Sh_{D_{eq}} \approx 10$ at ε=0.69.

The simultaneous presence of an axial flow leads to an increase of the Sherwood number with respect to the purely transverse flow case; the increase depends little on the Reynolds number Re_t. When Re_z increases from 0 to 100, $Sh_{D_{eq}}$ exhibits the largest increase at the intermediate porosity (0.50); for example, for Re_t=1, it increases by ~20% at ε=0.31, by ~35% at ε=0.50 and by ~30% at ε=0.69.

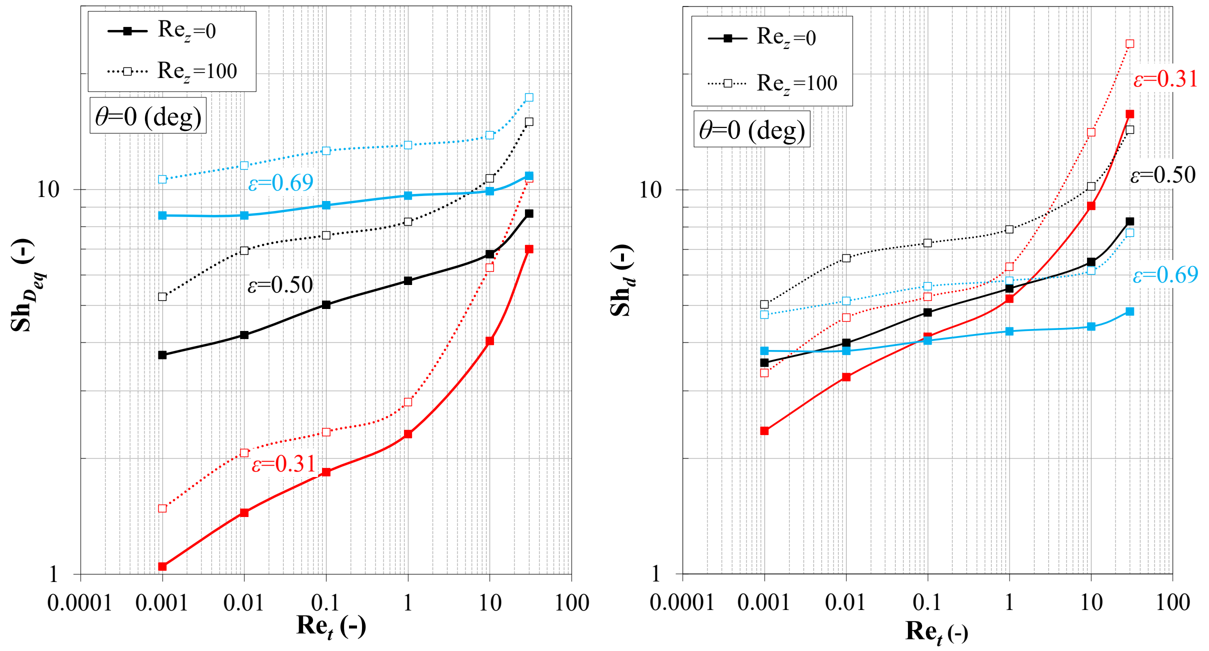

(a) (b)

Figure 11: Square fiber arrays: Sherwood number as a function of the transverse flow Reynolds number Re_t for Re_z=100 (mixed flow, dotted line) and Re_z=0 (purely transverse flow, solid line) and θ=0°. The Sherwood number is defined on the basis of the hydraulic diameter ($Sh_{D_{eq}}$) in graph (a) and of the fiber diameter (Sh_d) in graph (b).

Figure 11(b) reports the Sherwood number defined on the basis of the fiber diameter (Sh_d). Of course, when a specific porosity is considered, the considerations made above on $Sh_{D_{eq}}$ also apply to Sh_d since, in a log-log chart, the corresponding curves are simply translated with respect to each other by the constant factor $d/D_{eq}=(1-\varepsilon)/\varepsilon$, see Eq. (6). In particular, the curves for ε=0.50 do not change since, in this case, $d=D_{eq}$.

However, the relative magnitude of the Sherwood numbers relevant to different porosities change, and their monotonic dependence on the porosity is lost. For example, for Re_z=0, at Re_t=0.001 one has $(Sh_d)_{\varepsilon=0.69}>(Sh_d)_{\varepsilon=0.50}>(Sh_d)_{\varepsilon=0.31}$; at Re_t=1 one has $(Sh_d)_{\varepsilon=0.50}>(Sh_d)_{\varepsilon=0.31}>(Sh_d)_{\varepsilon=0.69}$; and at Re_t=10 one has $(Sh_d)_{\varepsilon=0.31}>(Sh_d)_{\varepsilon=0.50}>(Sh_d)_{\varepsilon=0.69}$. In the intermediate range $0.01<Re_t<1$, the highest Sh_d values are obtained for the intermediate porosity ε=0.50; this is consistent with the behavior reported in **Figure 4**(b) and **Figure 8** for purely axial flow and purely transverse flow at Re_t=0.5-1, where, unlike $Sh_{D_{eq}}$, Sh_d presents maxima when reported as a function of porosity.

Equivalent graphs for the hexagonal lattice are reported in **Figure 12**. A behavior of the Sherwood number qualitatively similar to that reported above for the square lattice can be observed, and similar considerations apply. The Sherwood number grows slowly with Re_t until $Re_t \approx 1$ and then increases more steeply. The simultaneous presence of an axial flow always results in the enhancement of mass transfer. As in the square lattice, for any Re_t and Re_z the Sherwood number $Sh_{D_{eq}}$ increases monotonically with the porosity ε. However, unlike in the square lattice case, here Sh_d decreases monotonically with ε, thus exhibiting a behavior opposite to that of $Sh_{D_{eq}}$. For the lowest porosity (0.30) the influence of the axial flow is much more marked than in the square lattice; for example, at ε=0.30 and Re_t=0.01, Sh_d increases from ~7 to ~17 as Re_z increases from 0 to 100.

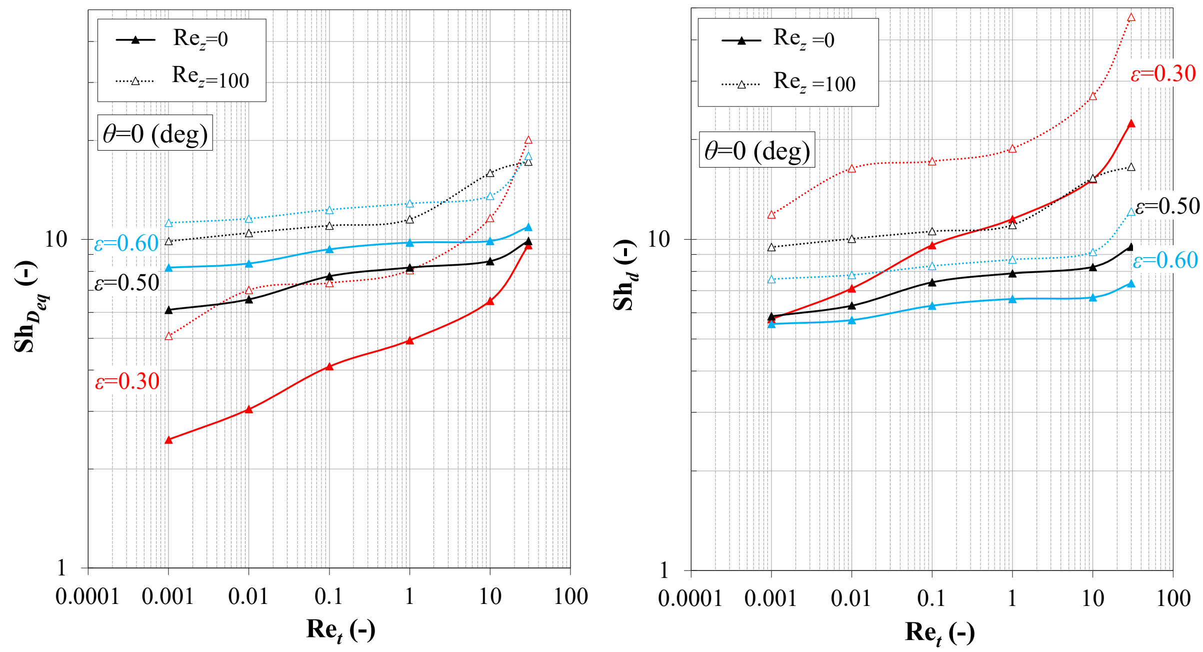

(a) (b)

Figure 12: Hexagonal fiber arrays: Sherwood number as a function of the transverse flow Reynolds number Re_t for Re_z=100 (mixed flow, dotted line) and Re_z=0 (purely transverse flow, solid line) and θ=0°. The Sherwood number is defined on the basis of the hydraulic diameter ($Sh_{D_{eq}}$) in graph (a) and of the fiber diameter (Sh_d) in graph (b).

3.3.3 Influence of the cross flow attack angle θ in mixed flow

Figure 13 reports the Sherwood number defined on the basis of the fiber diameter Sh_d as a function of the transverse Reynolds number Re_t, for different values of the flow attack angle θ. Each graph reports curves both for purely transverse flow (Re_z=0) and for mixed flow (Re_z=100).

In the figure, the left column (a, c, e) reports the graphs for the square lattice and the right column (b, d, f) those for the hexagonal lattice.

It can be observed that, independently of the flow condition (mixed or purely transverse flow), for θ=0° Sh$_d$ increases only moderately attaining values between ~5 and ~45 for Re$_t$=30, the highest values being attained at the lowest porosities (ε=0.3-0.31 according to the lattice).

The steepest increase and the highest values of Sh$_d$ are attained for flow attack angles of 22.5° (square lattice) and 15° (hexagonal lattice). An intermediate behavior is obtained at θ=45° (square lattice) and θ=30° (hexagonal lattice). Therefore, the Sherwood number is lower in the symmetry directions (0° and 45° for the square lattice, 0° and 30° for the hexagonal lattice) and higher at intermediate angles (22.5° and 15°, respectively, for the square and hexagonal lattices).

The reason for the Sherwood number being larger at flow attack angles which are not symmetry directions of the fiber array is illustrated in **Figure 14** and **Figure 15**, respectively for a square and a hexagonal lattice. These show the distribution of the normalized concentration C^*:

$$C^* = \frac{C - C_b}{\overline{C}_w - C_b} \tag{13}$$

in which, as discussed in Section 2.2, $\overline{C}_w$ is the wall-averaged solute concentration at the wall and C_b is the mass flow-weighted average of the solute concentration on an arbitrary cross section, i.e. the bulk concentration.

One can observe that, when the flow attack angle coincides with a symmetry direction of the fiber array (0° or 45° for the square lattice and 0° or 30° for the hexagonal one), the central impingement of the flow that separates from a fiber on the subsequent fiber causes a large stagnant-flow wake region to be formed and a thick concentration boundary layer to develop around each fiber. On the contrary, for non-symmetry flow attack angles (22.5° for the square lattice and 15° for the hexagonal lattice in the present examples), the separating flow reattaches farther downstream after "meandering" between fibers, the stagnant flow region is small and the concentration boundary layer is thin, which amounts to a larger mass transfer coefficient (Sherwood number) being attained. Note also that, for intermediate flow attack angles, **Figures 14**(b) and **15**(b), the directions of the applied forcing term (arrow) and of the mean flow (as indicated by the wake) do not coincide.

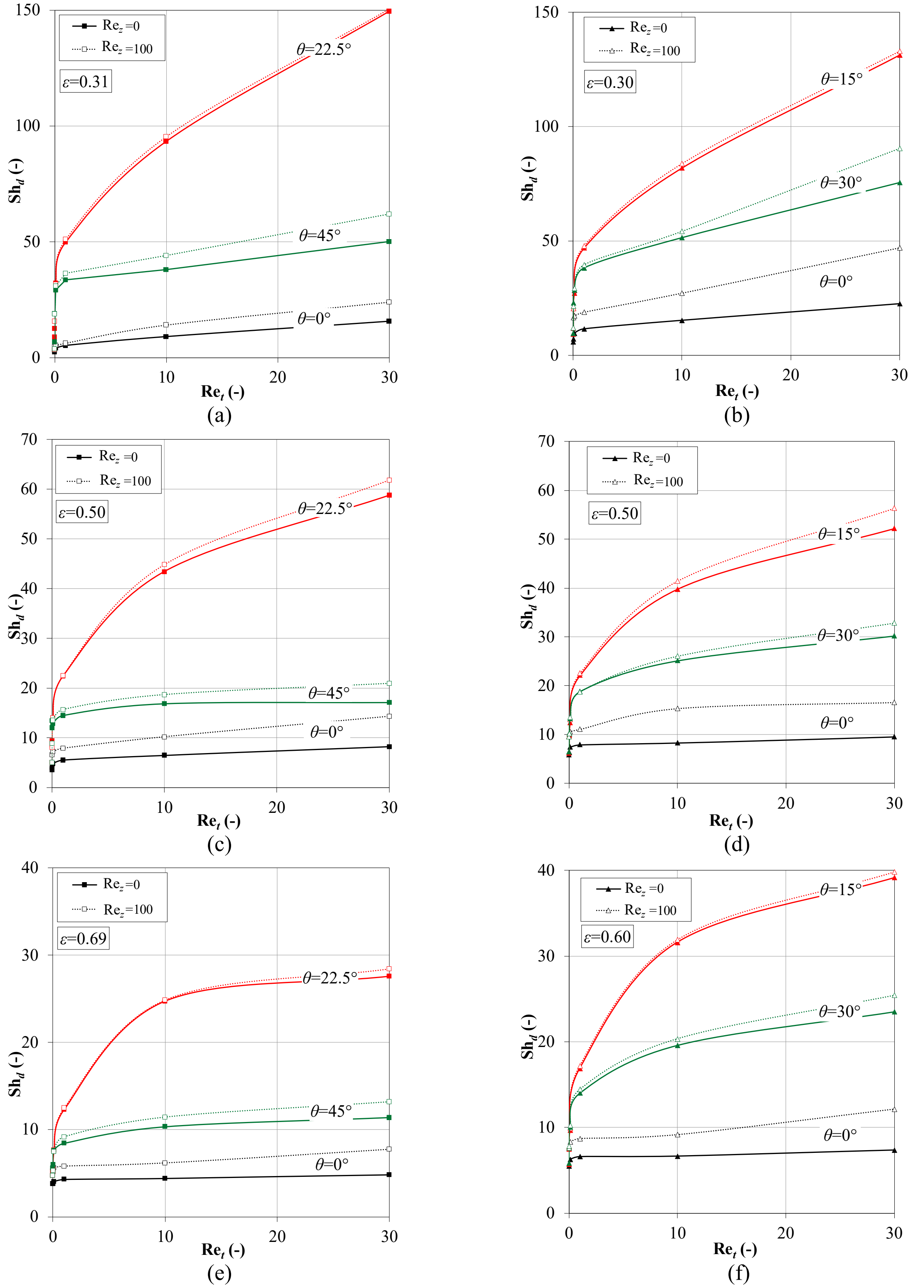

Figure 13: Sherwood number Sh_d, defined on the basis of the fiber diameter, as a function of the transverse flow Reynolds number Re_t in mixed flow at Re_z=100 (dotted line) and in purely transverse flow (solid line), for different values of θ. Left column (a, c, e): square arrays; right column (b, d, f): hexagonal arrays.

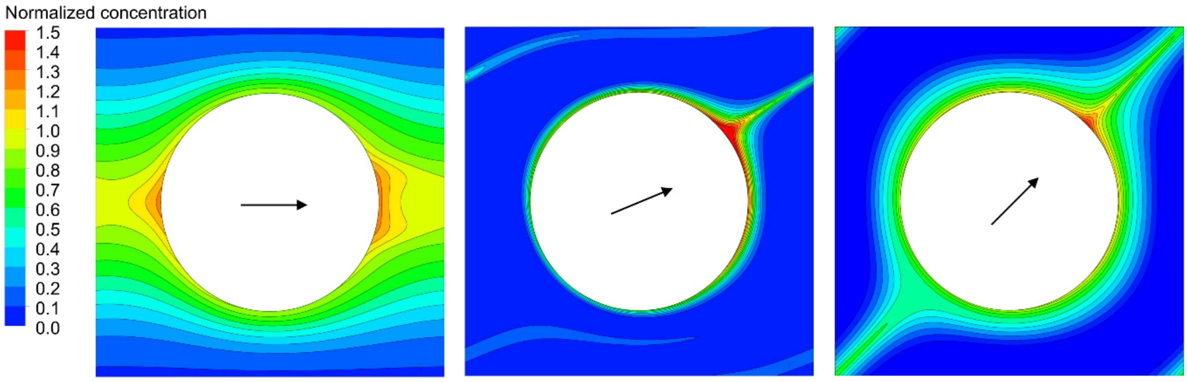

(a) (b) (c)

Figure 14: Maps of the normalized concentration in a cross-sectional plane for a square lattice, Re_z=0, Re_t=10, ε=0.69 and flow attack angles θ of 0° (a), 22.5° (b) and 45° (c).

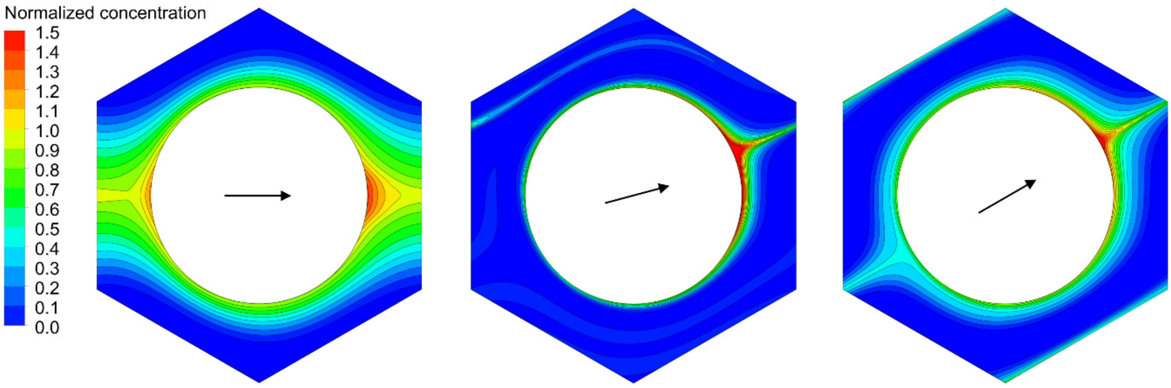

(a) (b) (c)

Figure 15: Maps of the normalized concentration in a cross-sectional plane for a hexagonal lattice, Re_z=0, Re_t=10, ε=0.60 and flow attack angles θ of 0° (a), 15° (b) and 30° (c).

4. Conclusions

The hydraulic and mass transfer characteristics of bundles of straight cylindrical fibers were investigated by Computational Fluid Dynamics. Both square and hexagonal regular fiber arrays were considered. The bundle porosity was made to vary between a value close to the theoretical minimum and a very high value close to the theoretical maximum of 1. Purely axial, purely transverse and mixed flows were investigated under the assumption of steady laminar conditions and the influence of the transverse flow attack angle was studied. In most cases, the flow and concentration fields were assumed to be fully developed and a two-dimensional computational domain was adopted. For some configurations, entry effects were also studied using a fully three-dimensional domain.

In purely axial flow, the axial Darcy permeability was found to increase strongly with the porosity ε, especially for large ε, and to be slightly larger for a square lattice than for a hexagonal one, especially at low porosities; the difference decreased with increasing ε and became negligible for ε>0.7.

In purely transverse flow, the transverse permeability also increased strongly with the porosity; up to $\varepsilon\approx0.6$ it was larger for a hexagonal than for a square lattice (a behaviour opposite to that of the axial permeability), the difference becoming negligible for larger porosities.

In mixed flow, the axial permeability K_z was not affected by the axial Reynolds number Re_z (as expected for a Darcy medium), but decreased significantly with the transverse Reynolds number Re_t provided this exceeded a value of ~1; the effect was larger at low porosities and larger for a square than for a hexagonal lattice. On the other hand, both for square and hexagonal lattices the transverse permeability K_t was not affected by the axial flow Reynolds number Re_z. Provided the transverse flow Reynolds number Re_t did not exceed the value of ~10, K_t was not affected either by Re_t (i.e., the medium was Darcian) or by the flow attack angle θ (i.e., the medium was isotropic with respect to directions lying in a cross-sectional plane).

In regard to mass transfer, in purely axial flow the Sherwood number Sh_d based on the fiber diameter d (and thus the mass transfer coefficient), once plotted as a function of the porosity, exhibited a bell-shaped behaviour, with a maximum of ~12 at $\varepsilon\approx0.38$ for the hexagonal lattice and of ~5 at $\varepsilon\approx0.6$ for the square lattice. On the other hand, the Sherwood number $Sh_{D_{eq}}$ based on the hydraulic diameter D_{eq} exhibited a monotonically increasing behaviour and diverged for $\varepsilon\rightarrow1$.

In purely transverse flow, a qualitatively similar dependence of Sh_d from the porosity was obtained. In particular, for a flow attack angle $\theta=0°$, in a hexagonal lattice the maximum value of Sh_d was ~12.6 and was attained at $\varepsilon\approx0.25$ while, in a square lattice, Sh_d attained a maximum of ~5.5 at $\varepsilon\approx0.45$. Unlike the Darcy permeability, the Sherwood number was found to depend strongly on the flow attack angle even at transverse Reynolds numbers as low as 0.01, denoting a strong anisotropy of the medium in regard to mass transfer. In particular, for both lattices Sh_d exhibited absolute or relative minima at values of θ corresponding to directions of symmetry (0° and 45° for a square lattice and 0° and 30° for a hexagonal one), while it was much larger at some intermediate angle (~22.5° for a square lattice and ~15° for a hexagonal one).

In mixed flow, superimposing an axial flow at Re_z=100 on a pre-existing transverse flow caused the Sherwood number to increase significantly, in complex dependence on geometry (square vs. hexagonal lattice), porosity and transverse flow Reynolds number Re_t.

For the case of purely axial flow, a square lattice, and a few values of the porosity, entry effects were also investigated by assuming simultaneously developing flow and concentration boundary layers. The Darcy permeability K_z was computed as a function of the dimensionless distance from the inlet, $z/(\mathrm{Re}_z \cdot D_{eq})$, and the Sherwood number Sh_d was computed as a function of $z/(\mathrm{Re}_z \cdot \mathrm{Sc} \cdot D_{eq})$ (reciprocal of the Graetz number).

Hydrodynamic entry effects were found to be limited to a small inlet region of the bundle, between 5 and 50 hydraulic diameters, a length utterly negligible with respect to the module length in most applications. In regard to mass transfer, entry effects were found to be important in the presence of large Schmidt numbers, because in this case the Péclet number may well be very large, so that the entry length becomes comparable or even larger than the size of a typical mass transfer module.

Several of the present predictions (notably pertaining to the Darcy permeability in both axial and transverse flow and to the Sherwood number in axial flow) were compared with experimental or computational results from the literature; in all cases a good agreement was observed.

Acknowledgments

Part of this work was carried out with the financial support of the *Programma Operativo Nazionale Ricerca e Innovazione 2014-2020 (CCI 2014IT16M2OP005), Fondo Sociale Europeo, Azione I.1 “Dottorati Innovativi con caratterizzazione Industriale”*.

Nomenclature

C	solute concentration (mol m^{-3})
C^*	normalized concentration (-)
D	solute diffusion coefficient (m^2 s^{-1})
D_{eq}	hydraulic diameter (m)
d	outer diameter of the fiber (m)
$\vec{f}$	forcing term compensating the large-scale pressure gradient (Pa)
Gz	Graetz number
J	local mass flux at the wall (mol m^{-2} s^{-1})
K	Darcy permeability based on the superficial velocity (m^2)
p	pressure (Pa)
Pe	Péclet number
Re_z	longitudinal Reynolds number (-)
Re_t	transverse Reynolds number (-)
S	wet surface of the computational domain (m^2)
S_C	source term compensating the large-scale concentration gradient (mol m^{-3} s^{-1})
Sc	Schmidt number (-)
Sh_d	Sherwood number defined on the basis of the fiber diameter (-)
$Sh_{D_{eq}}$	Sherwood number defined on the basis of the hydraulic diameter (-)
t	cross-flow direction (m)
U	local shell-side mass transfer coefficient (m s^{-1})
$\vec{u}$	superficial velocity vector (m s^{-1})
V	volume (m^3)
x, y	Cartesian coordinates in cross section orthogonal to the fibers (m)
z	Cartesian coordinate parallel to the fibers (m)

Greek symbols

$\vec{\gamma}$	unit vector characterizing the direction of the mean superficial velocity (-)

ε	porosity (-)
θ	cross-flow attack angle (between $\vec{\sigma}$ and the x axis) (°)
μ	dynamic viscosity (Pa s)
$\vec{\xi}$	unit vector of the generic direction (-)
ρ	density (kg m^{-3})
$\vec{\sigma}$	unit vector characterizing the direction of the imposed forcing term (-)

Subscripts

b	bulk (mass flow averaged)
d	fiber diameter
D_{eq}	hydraulic diameter
t	transverse (lying in a plane orthogonal to the fibers)
tot	total
w	wall (external surface of the fibers)
x, y, z	coordinates
σ	direction of the imposed forcing term
∞	fully developed value

Averages

$\overline{}$	surface average
$\langle \ \rangle$	volume average

Acronyms

CFD	Computational Fluid Dynamics
FV	Finite volume

References

[1] M.H. Ibrahim, M.H. El-Naas, Z. Zhang, B. Van Der Bruggen, CO2 Capture Using Hollow Fiber Membranes: A Review of Membrane Wetting, Energy and Fuels. 32 (2018) 963–978. https://doi.org/10.1021/acs.energyfuels.7b03493.

[2] L.Z. Zhang, Z.X. Li, T.S. Zhong, L.X. Pei, Flow maldistribution and performance deteriorations in a cross flow hollow fiber membrane module for air humidification, J. Memb. Sci. 427 (2013) 1–9. https://doi.org/10.1016/j.memsci.2012.09.030.

[3] C.H. Yun, R. Prasad, A.K. Guha, K.K. Sirkar, Hollow Fiber Solvent Extraction Removal of Toxic Heavy Metals from Aqueous Waste Streams, Ind. Eng. Chem. Res. 32 (1993) 1186–1195.

[4] M. Sheikh, M. Reig, X. Vecino, J. Lopez, M. Rezakazemi, C.A. Valderrama, J.L. Cortina, Liquid–Liquid membrane contactors incorporating surface skin asymmetric hollow fibres of poly(4-methyl-1-pentene) for ammonium recovery as liquid fertilisers, Sep. Purif. Technol. 283 (2022) 120212. https://doi.org/10.1016/j.seppur.2021.120212.

[5] X.Y. Chen, S. Kaliaguine, D. Rodrigue, Polymer hollow fiber membranes for gas separation: A comparison between three commercial resins, AIP Conf. Proc. 2139 (2019) 1–15. https://doi.org/10.1063/1.5121669.

[6] Y. Dou, X. Dong, Y. Ma, P. Ge, C. Li, A. Zhu, Q. Liu, Q. Zhang, Hollow fiber ultrafiltration membranes of poly (biphenyl-trifluoroacetone), J. Memb. Sci. 659 (2022) 120779. https://doi.org/10.1016/j.memsci.2022.120779.

[7] C. Ronco, W.R. Clark, Haemodialysis membranes, Nat. Rev. Nephrol. 14 (2018) 394–410.

[8] O.O. Teber, A.D. Altinay, S.A.N. Mehrabani, R.S. Tasdemir, B. Zeytuncu, E.A. Genceli, E. Dulekgurgen, K. Pekkan, İ. Koyuncu, Polymeric hollow fiber membrane oxygenators as artificial lungs: A review, Biochem. Eng. J. 180 (2022). https://doi.org/10.1016/j.bej.2022.108340.

[9] C.F. Wan, T. Yang, G.G. Lipscomb, D.J. Stookey, T.S. Chung, Design and fabrication of hollow fiber membrane modules, J. Memb. Sci. 538 (2017) 96–107. https://doi.org/10.1016/j.memsci.2017.05.047.

[10] E.L. Cussler, Diffusion: Mass Transfer in Fluid Systems, Third Ed., Cambridge University Press, 2009.

[11] M. -C Yang, E.L. Cussler, Designing hollow-fiber contactors, AIChE J. 32 (1986) 1910–1916. https://doi.org/10.1002/aic.690321117.

[12] S.R. Wickramasinghe, M.J. Semmens, E.L. Cussler, Mass transfer in various hollow fiber geometries, J. Memb. Sci. 69 (1992) 235–250. https://doi.org/10.1016/0376-7388(92)80042-I.

[13] R. Prasad, K.K. Sirkar, Dispersion-free solvent extraction with microporous hollow-fiber modules, AIChE J. 34 (1988) 177–188. https://doi.org/10.1002/aic.690340202.

[14] M.J. Costello, A.G. Fane, P.A. Hogan, R.W. Schofield, The effect of shell side hydrodynamics on the performance of axial flow hollow fibre modules, J. Memb. Sci. 80 (1993) 1–11. https://doi.org/10.1016/0376-7388(93)85127-I.

[15] H. Kreulen, C.A. Smolders, G.F. Versteeg, W.P.M. van Swaaij, Microporous hollow fibre membrane modules as gas-liquid contactors. Part 1. Physical mass transfer processes. A specific application: Mass transfer in highly viscous liquids, J. Memb. Sci. 78 (1993) 197–216. https://doi.org/10.1016/0376-7388(93)80001-E.

[16] J. Günther, P. Schmitz, C. Albasi, C. Lafforgue, A numerical approach to study the impact of packing density on fluid flow distribution in hollow fiber module, J. Memb. Sci. 348 (2010) 277–286. https://doi.org/10.1016/j.memsci.2009.11.011.

[17] S. Eloot, D. De Wachter, I. Van Tricht, P. Verdonck, Computational flow modeling in hollow-fiber dialyzers, Artif. Organs. 26 (2002) 590–599. https://doi.org/10.1046/j.1525-1594.2002.07081.x.

[18] N. Cancilla, L. Gurreri, G. Marotta, M. Ciofalo, A. Cipollina, A. Tamburini, G. Micale, CFD prediction of shell-side flow and mass transfer in regular fiber arrays, Int. J. Heat Mass Transf. 168 (2021) 120855.

[19] P.W. Dierickx, D.S. De Wachter, P.R. Verdonck, Two-dimensional finite element model for oxygen transfer in cross-flow hollow fiber membrane artificial lungs, Int. J. Artif. Organs. 24 (2001) 628–635. https://doi.org/10.1177/039139880102400904.

[20] J. Zhang, X. Chen, J. Ding, K.H. Fraser, M.E. Taskin, B.P. Griffith, Z.J. Wu, Computational Study of the Blood Flow in Three Types of 3D Hollow Fiber Membrane Bundles, J. Biomech. Eng. 135 (2013) 1–12. https://doi.org/10.1115/1.4025717.

[21] S. Buetehorn, D. Volmering, K. Vossenkaul, T. Wintgens, M. Wessling, T. Melin, CFD simulation of single- and multi-phase flows through submerged membrane units with irregular fiber arrangement, J. Memb. Sci. 384 (2011) 184–197. https://doi.org/10.1016/j.memsci.2011.09.022.

[22] V. Chen, M. Hlavacek, Application of Voronoi tessellation for modeling randomly packed hollow-fiber bundles, AIChE J. 40 (1994) 606–612. https://doi.org/10.1002/aic.690400405.

[23] J.D. Rogers, R.L. Long, Modeling hollow fiber membrane contactors using film theory, Voronoi tessellations, and facilitation factors for systems with interface reactions, J. Memb. Sci. 134 (1997) 1–17. https://doi.org/10.1016/S0376-7388(97)00074-4.

[24] J. Wu, V. Chen, Shell-side mass transfer performance of randomly packed hollow fiber modules, J. Memb. Sci. 172 (2000) 59–74.

[25] O. Emersleben, Das Darcysche Filtergesetz, Phys. Z. 26 (1925).

[26] R.R. Sullivan, Further study of the flow of air through porous media, J. Appl. Phys. 12 (1941) 503–508. https://doi.org/10.1063/1.1712932.

[27] R.R. Sullivan, Specific surface measurements on compact bundles of parallel fibers, J. Appl. Phys. 13 (1942) 725–730. https://doi.org/10.1063/1.1714824.

[28] O.E. Dwyer, H.C. Berry, Laminar-Flow Heat Transfer for in- Line Flow Through Unbaffled Rod Bundles, Nucl. Sci. Eng. 42 (1970) 81–88. https://doi.org/10.13182/nse70-a19330.

[29] L. Bao, G.G. Lipscomb, Mass transfer in axial flows through randomly packed fiber bundles with constant wall concentration, J. Memb. Sci. 204 (2002) 207–220. https://doi.org/10.1016/S0376-7388(02)00043-1.

[30] A.S. Sangani, A. Acrivos, Slow flow past periodic arrays of cylinders with application to heat transfer, Int. J. Multiph. Flow. 8 (1982) 193–206. https://doi.org/10.1016/0301-9322(82)90029-5.

[31] O. Bergelin, G. Brown, H. Hull, F. Sullivan, Heat transfer and fluid friction during viscous flow across banks of tubes: III–a study of tube spacing and tube size, ASME Trans. 72 (1950) 881–888.

[32] A.A. Kirsch, N.A. Fuchs, Studies on fibrous aerosol filters-ii. pressure drops in systems of parallel cylinders, Ann. Occup. Hyg. 10 (1967) 23–30. https://doi.org/10.1093/annhyg/10.1.23.

[33] L. Skartsis, J.L. Kardos, B. Khomami, Resin flow through fiber beds during composite manufacturing processes. Part I: Review of newtonian flow through fiber beds, Polym. Eng. Sci. 32 (1992) 221–230. https://doi.org/10.1002/pen.760320402.

[34] L. Skartsis, B. Khomami, J.L. Kardos, Resin flow through fiber beds during composite manufacturing processes. Part II: Numerical and experimental studies of newtonian flow through ideal and actual fiber beds, Polym. Eng. Sci. 32 (1992) 231–239. https://doi.org/10.1002/pen.760320403.

[35] E.M. Sparrow, A.L. Loeffler, Longitudinal laminar flow between cylinders arranged in regular array, AIChE J. 5 (1959) 325–330. https://doi.org/10.1002/aic.690050315.

[36] I. Noda, C.C. Gryte, Mass Transfer in Regular Arrays of Hollow Fibers in Countercurrent Dialysis, AIChE J. 25 (1979) 113–122.

[37] L. Bao, G.G. Lipscomb, Well-developed mass transfer in axial flows through randomly packed fiber bundles with constant wall flux, Chem. Eng. Sci. 57 (2002) 125–132. https://doi.org/10.1016/S0009-2509(01)00368-2.

[38] O. Miyatake, H. Iwashita, Laminar-flow heat transfer to a fluid flowing axially between cylinders with a uniform wall heat flux, Int. J. Heat Mass Transf. 34 (1991) 322–327.

[39] J. Happel, Viscous flow relative to arrays of cylinders, AIChE J. 5 (1959) 174–177.

https://doi.org/10.1002/aic.690050211.

[40] T. Miyagi, Viscous Flow at Low Reynolds Numbers past an Infinite Row of Equal Circular Cylinders, J. Phys. Soc. Japan. 13 (1958) 493–496. https://doi.org/10.1143/JPSJ.13.493.

[41] K. Ishimi, S. Koroyasu, H. Hikita, Mass transfer in creeping flow past periodic arrays of cylinders, J. Chem. Eng. Japan. 20(5) (1987) 492–498.

[42] K.A. Antonopoulos, Heat transfer in tube assemblies under conditions of laminar axial, transverse and inclined flow, Int. J. Heat Fluid Flow. 6 (1985) 193–204. https://doi.org/10.1016/0142-727X(85)90010-4.

[43] J. Wilk, Heat/mass transfer analogy in the case of convective fluid flow through minichannels, Int. J. Therm. Sci. 156 (2020) 106467. https://doi.org/10.1016/j.ijthermalsci.2020.106467.

[44] O. Miyatake, H. Iwashita, Laminar-flow heat transfer to a fluid flowing axially between cylinders with a uniform surface temperature, Int. J. Heat Mass Transf. 33 (1990) 417–425. https://doi.org/10.1252/kakoronbunshu.13.152.

[45] L. Bao, B. Liu, G.G. Lipscomb, Entry mass transfer in axial flows through randomly packed fiber bundles, AIChE J. 45 (11) (1999) 2346–2356. https://doi.org/10.1016/S0927-5193(03)80004-9.

[46] D.W. Green, R.H. Perry, Perry’s Chemical Engineers’ Handbook, 8th ed., McGraw-Hill, New York, 2008.

[47] V. Vitagliano, P.A. Lyons, Diffusion Coefficients for Aqueous Solutions of Sodium Chloride and Barium Chloride, J. Am. Chem. Soc. 78 (1956) 1549–1552. https://doi.org/10.1021/ja01589a011.

[48] E. Klein, F. Holland, A. Lebeouf, A. Donnaud, J.K. Smith, Transport and mechanical properties of hemodialysis hollow fibers, J. Memb. Sci. 1 (1976) 371–396. https://doi.org/10.1016/S0376-7388(00)82283-8.

[49] A. Tamburini, G. La Barbera, A. Cipollina, M. Ciofalo, G. Micale, CFD simulation of channels for direct and reverse electrodialysis, Desalin. Water Treat. 48 (2012) 370–389. https://doi.org/10.1080/19443994.2012.705084.

[50] A.S. Sangani, C. Yao, Transport processes in random arrays of cylinders. II. Viscous flow, Phys. Fluids. 31 (1988) 2435–2444. https://doi.org/10.1063/1.866596.

[51] R.K. Shah, A Correlation for Laminar Hydrodynamic Entry Length Solutions for Circular and Noncircular Ducts, J. Fluids Eng. 100 (1978) 177–179.

[52] D.P. Fleming, E.M. Sparrow, Flow in the hydrodynamic entrance region of ducts of

arbitrary cross section, J. Heat Transfer. 91 (1969) 345–354. https://doi.org/10.1115/1.3580173.

[53] E.M. Sparrow, S.H. Lin, T.S. Lundgren, Flow development in the hydrodynamic entrance region of tubes and ducts, Phys. Fluids. 7 (1964) 338–347. https://doi.org/10.1063/1.1711204.

[54] W.M. Kays, M.E. Crawford, Convective heat and mass transfer, Third Edit, McGraw-Hill, 1993. https://doi.org/10.1017/CBO9780511800603.

[55] R. Siegel, E.M. Sparrow, T.M. Hallman, Steady Laminar Heat Transfer in a Circular Tube with Prescribed Wall Heat Flux, Appl. Sci. Res. 7 (1958) 386–392. https://doi.org/10.1252/kakoronbunshu1953.38.144.

[56] P.S. Lee, S. V. Garimella, D. Liu, Investigation of heat transfer in rectangular microchannels, Int. J. Heat Mass Transf. 48 (2005) 1688–1704. https://doi.org/10.1016/j.ijheatmasstransfer.2004.11.019.

[57] P.S. Lee, S. V. Garimella, Thermally developing flow and heat transfer in rectangular microchannels of different aspect ratios, Int. J. Heat Mass Transf. 49 (2006) 3060–3067. https://doi.org/10.1016/j.ijheatmasstransfer.2006.02.011.

[58] M.L. La Cerva, M. Di Liberto, L. Gurreri, A. Tamburini, A. Cipollina, G. Micale, M. Ciofalo, Coupling CFD with a one-dimensional model to predict the performance of reverse electrodialysis stacks, J. Memb. Sci. 541 (2017) 595–610. https://doi.org/10.1016/j.memsci.2017.07.030.

[59] C.H.K. Williamson, Vortex dynamics in the cylinder wake, Annu. Rev. Fluid Mech. 28 (1996) 477–539. https://doi.org/10.1146/annurev.fl.28.010196.002401.